



## Algebraic Filtering of Surfaces from 3D Medical Images with Julia

Miroslav Jirík<sup>1,3</sup> , Alberto Paoluzzi<sup>2</sup> ,

<sup>1</sup> Charles University, Faculty of Medicine in Pilsen, Biomedical Center, [jirik@lfp.cuni.cz](mailto:jirik@lfp.cuni.cz)

<sup>2</sup>Roma Tre University, Department of Mathematics and Physics, [paoluzzi@dia.uniroma3.it](mailto:paoluzzi@dia.uniroma3.it)

<sup>3</sup>NTIS, Faculty of Applied Sciences, University of West Bohemia,

Corresponding author: Miroslav Jirík, [jirik@lfp.cuni.cz](mailto:jirik@lfp.cuni.cz)

**Abstract.** In this paper we introduce a novel algebraic filter, based on algebraic topology methods, to extract and smooth the boundary surface of any subset of voxels arising from the segmentation of a 3D medical image. The input of the Linear Algebraic Representation (LAR) Surface extraction filter (LAR-SURF) is defined as a *chain*, i.e. a vector from a linear space of chains, here subsets of voxels, represented in coordinates as a sparse binary vector. The output is produced by a linear mapping between spaces of 3- and 2-chains, given by the boundary operator  $\partial_3 : C_3 \rightarrow C_2$ . The only data structures used by this approach are sparse arrays with one or two indices, i.e. sparse vectors and sparse matrices. This work is based on LAR algebraic methods and is implemented in Julia language, natively supporting parallel computing on hybrid hardware architectures.

**Keywords:** Medical 3D, Computational Topology, Linear Algebraic Representation, LAR, Julia, Surface Extraction

**DOI:** <https://doi.org/10.3722/cadaps.2020.xxx-yyy>

### 1 Introduction

Isosurface extraction to produce geometric models of surfaces from volumetric data is important in many applications. It is often used for interactive visualization of medical data and/or for flow modeling [21].

The most popular algorithm used for surface extraction from volume images is called *Marching Cubes* (MC). The algorithm was described by Lorentsen and Cline [13] in 1987. A survey of algorithms MC-inspired has been published in 2006 [15]. The algorithm is based on considering the small cubes defining the volumetric image. Each corner vertex of each cube is related to input volumetric data, typically as average of the incident voxel data. MC traverses the data cube-by-cube, and constructs a triangulated iso-surface by using a lookup table depending on pattern of transitions between values of adjacent cube vertices. The main disadvantages of this method are time requirements, ambiguity, and holes generation. Some of them were discovered shortly after the algorithm was introduced. In 1991 Nielson and Hamman described an Asymptotic Decider to solve

the ambiguity problem on the faces of the cube. Natarajan noted that the ambiguity problem also occurs with uniform samples [14]. In 1995 Chernyaev extended the number of lookup cases to 33 [5]. More recently, the algorithm was updated by Custodio, Pescos, and Silva to enhance the quality of iso-surface triangulation [7].

Some alternative methods have been developed, including a method for surface extraction from a grid of field values using particle attraction; a system was described by Crossno and Angel in [6]. A graph processing that tracks the boundary cell-face adjacencies is described in [12]. Some parallel algorithms for iso-surface extraction are discussed in [1]. A data-parallel algorithm, implemented in OpenCL, that runs entirely on the GPU is presented in [23]. A Linear Algebraic Representation approach, parallelized using the OpenCL framework on Linux, was introduced in [16].

In the present paper we discuss a distributed approach for surface extraction, where the LAR-SURF (Linear Algebraic Representation Surface Extraction) filter is based on basic linear algebra and algebraic topology, using linear spaces  $C_p$  of chains (of cells) of dimension  $0 \leq p \leq 3$  and the boundary matrix  $[\partial_3] : C_3 \rightarrow C_2$ .

Input volumetric data are represented by a 3D voxel array and can be generated, e.g., by segmentation of a computed tomography (left image of Fig. 3). A decomposition of the input volumetric data into small submatrices called *bricks* is performed, then the binary coordinate vector of each *segment* (mathematically, a chain) of voxels is generated, and its boundary is computed by multiplication times the boundary matrix. The resulting output is a sparse binary vector holding the LAR representation of the boundary surface. Such embarrassing parallel data decomposition is used to independently compute within each of the bricks the boundary patches, that are finally joined and smoothed via the Taubin algorithm [26].

The present paper is organized as follows. Section 2 provides the basic topological and geometrical concepts needed to understand the LAR-SURF method, including the building of boundary matrices, the map from Cartesian indices to linear indices, and the Taubin smoothing method. Section 3 discusses the parametric design of the unit block filtered by the parallel algorithm, including the block decomposition, the sparsity rate of the used sparse arrays, and the block-level parallelism. Section 4 is related to the algorithm implementation in Julia, and in particular to a discussion of the parallel workflow. Section 5 presents some examples of algorithm execution on the liver and the hepatic portal system. Section 6 shortly describes the next extensions of this approach, in particular the implementation with Julia's support for GPU parallelism and the multi-segmentation of medical images.

## 2 Background

Some basic concepts of solid modeling, and in particular the foundational idea of representation scheme, as well as few basic concepts of algebraic topology, are shortly introduced in this section, including the computation of the matrix of a boundary operator between chain spaces.

### 2.1 Representation Scheme

A *representation scheme* for solid modeling is a mapping between a space of mathematical models and a space of symbolic representations, like generated by a formal grammar. Solid pointsets (i.e., “*r*-sets”) are defined in [20] as compact (bounded and closed) regular and semianalytic<sup>1</sup> subsets of the *d*-space. A large number of representation schemes were defined in the past forty years, including the two main classes of (a) *boundary representations* (“*B*-reps”), where the solid model is represented through a representation of its boundary elements, i.e. faces, edges and vertices, and (b) *decompositional/enumerative representations* [20], that are a decomposition of either the object or the embedding space, respectively, into a well-defined *cellular complex*. In particular, a boundary representation provides a cellular decomposition of the object’s boundary into *cells* of dimension zero (vertices), one (edges), and two (faces). Medical imaging can be classified as the *enumerative*

---

<sup>1</sup>Semianalytic sets, studied in algebraic geometry, are solutions of systems of polynomials; are closed under (regularized) set union, intersection and difference, and so constitute a Boolean algebra [18].

representation of cellular decompositions of organs and tissues of interest [16], in particular, as subsets of 3D volume elements (voxels) from the 3D medical image.

## 2.2 Linear Algebraic Representation

The *Linear Algebraic Representation* (LAR), introduced in [9], aims to represent the *chain complex* [8, 17] generated by a piecewise-linear *geometric complex* embedded either in 2D or in 3D. This representation provides a minimal characterization of geometry and topology of a cellular complex, through (a) the embedding mapping  $\mu : C_0 \rightarrow \mathbb{E}^d$  of 0-cells (vertices), and (b) a description of  $d$ -cells and/or  $(d - 1)$ -cells as subsets of vertices. When evaluated, it is able to return the whole chain complex:

$$C_\bullet = (C_p, \partial_p) := C_3 \xleftarrow[\partial_3]{\delta_2} C_2 \xleftarrow[\partial_2]{\delta_1} C_1 \xleftarrow[\partial_1]{\delta_0} C_0. \quad (1)$$

i.e., the whole sequence of graded linear *chain spaces*  $C_p$ , and any linear *boundary*  $\partial_p$  and *coboundary*  $\delta_p$  map, with  $\delta_p = \partial_{p-1}^\top$  between them. The *domain* of LAR is the set of **chain complexes** generated by cell  $d$ -complexes ( $2 \leq d \leq 3$ ). The computer *representations* of LAR are **sparse binary matrices** to represent both the operators and the bases of chain spaces. Note that in algebraic topology a  $p$ -chain is defined as a linear combination of  $p$ -cells with scalars from a field. When the scalar coefficients are from  $\{-1, 0, +1\}$ , a chain may represent *any (oriented) subset of cells* from the cellular complex. Scalars from  $\{0, 1\}$  are used for non-oriented complexes.

We may, therefore, get the  $(p - 1)$ -boundary  $\partial_p c_p$  of *any*  $p$ -chain  $c_p$ , by multiplication of the coordinate representation  $[\partial_p]$  of the boundary operator times the coordinate representation  $[c_p]$  of the chain in terms of such scalars, i.e. by a matrix-vector product  $[\partial_p][c_p]$ .

It is possible to show that the LAR representation scheme is very expressive, i.e. that it has a large domain, including collections of: line segments, quads, triangles, polygons, meshes; pixels, voxels, volume images; B-reps, enumerative and decompositional representations of solids. In this paper we apply LAR methods to computation of boundary representations of solid models from segmentation (labeling) of 3D medical images. To display a triangulation of boundary faces in their proper position in space, the information required is contained in the *geometric chain complex* (GCC):

$$\mu : C_0 \rightarrow \mathbb{E}^3, (\delta_0, \delta_1, \delta_2) \equiv (\text{geom}, \text{top}) = (\text{V}, (\text{EV}, \text{FE}, \text{CF}))$$

Note that ordered pairs of letters from V,E,F,C, correspond to *Vertices*→*Edges*→*Faces*→*Cells* into the *Column*→*Row* order of matrix maps of linear operators. The GCC allows to transform the (possibly non connected) boundary 2-cycle of manifold surfaces as a standard B-rep [22]. The geometry *geom* is given by the embedding matrix *V* of vertices (0-cells); the topology *top* by the three sparse matrices (EV, FE, CF) of coboundaries  $(\delta_0, \delta_1, \delta_2)$  of the chain complex describing a space arrangement [19].

### Construction of boundary matrix $\partial_d$

First, let us fix an ordering for the cells of a partition of input data, i.e., the matrix of vertex coordinates *V*, and the arrays of arrays of vertex indices specifying edges *EV*, pixels *FV*, and voxels *CV*. i.e. for each 0-, 1-, 2-, and 3-elements of a cell partition *V,E,F,C* of a 3D image. These orderings fix the  $p$ -bases for the linear spaces  $C_p$  of  $p$ -chains ( $0 \leq p \leq 3$ ). The matrix  $M_p = (m_{i,j})$  is called the *characteristic matrix* of the  $p$ -basis, where each  $p$ -cell is expressed as a subset of vertices (0-cells), so that  $m_{i,j} = 1$  if and only if the  $j$ -th 0-cell  $c_0^j$  belongs to the boundary of  $i$ -th  $p$ -cell  $m_{i,j}$ , and  $m_{i,j} = 0$  otherwise.

The computation of a boundary matrix  $[\partial_p]$  begins by computing the compatible product of the two characteristic matrices  $M_{p-1} M_p^t$ . Let us note that the product of binary matrices is not binary, so by computing

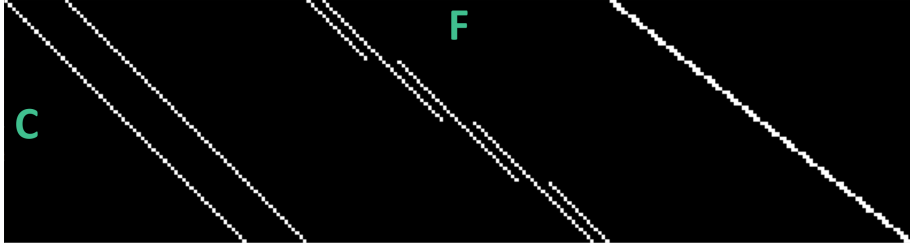


**Figure 1:** The binary image of *sparse coboundary matrix*  $[\delta_2] = [\partial_3]^t : C_2 \rightarrow C_3$ , built for a small volumetric data (or a brick) with shape  $(4, 4, 4)$ . Note that the number of rows equates the size  $4 \times 4 \times 4 = 64$  of the voxel set; the number of columns is  $d n (1 + n)^{d-1} = 3 \times 4 \times 25 = 300$ . Of course, the number of non-zeros per row (cardinality of the facet set of a single voxel) is six, whereas the number of non-zeros per column is two, but on boundary facets. The letter F stands for *Faces*, on matrix columns, and the C stands for *Cells* (3-cells) on matrix rows.

the (sparse) matrix product  $(M_{p-1} M_p^t) = (n_{i,j})$ , with  $n_{i,j} = \sum_k m_{i,k} m_{k,j}$ , we get for each  $n_{i,j}$  the *number of vertices* shared by  $c_{p-1}^i$  and  $c_p^j$ . When this number equates the cardinality of  $c_{p-1}^i$ , this elementary chain is contained on the boundary of  $c_p^j$ . In volume imaging data, made by cubic 3-cells and square 2-cells between adjacent pairs of 3-cells, everywhere we get  $n_{i,j} = 4$ , we may state  $c_2^i \subset \partial c_3^j$ . Therefore, in each  $i$  row of  $M_2 M_3^t = (n_{i,j})$ , we have exactly *six column* where  $n_{i,j} = 4$ , since a cube (3-chain) has six boundary faces (2-chains). Look for this purpose at the rows of matrix in Figure 1. The unit incidence coefficients in  $[\partial_3]$  are accordingly located by filtering the elements with value 4. All the other matrix element are set to 0.

Finally, consider the linear graded boundary operator  $\partial_p : C_p \rightarrow C_{p-1}$ . As such, it contains by columns the representation of domain basis elements, expressed as a linear combination of the basis elements of the range space. Therefore, the operator matrix  $[\partial_d]$  is readily obtained by setting  $[\partial_d](i, j) = 1$  if  $n_{i,j} = 4$  and  $[\partial_d](i, j) = 0$  otherwise. Of course, it will contain six non-zero elements for the column. It may be worth remembering every 3-cell (voxel) of the volumetric data has exactly six 2-faces.

It is possible to show that all the interesting relations of incidence/adjacency between cells of different dimensions can be both computed and efficiently queried by pairwise computing some matrix products, with one of terms possibly transposed, using only the two boundary and coboundary operator matrices  $[\partial_p]$  and  $[\delta_p]$ , and where  $[\delta_p] = [\partial_p^\top]$ . We may also show that such matrices are *very sparse*, with their sparseness growing rapidly with the dimensions (see Section 3.2). The pattern of non-zeros in matrix  $[\partial_3]$  corresponding to a brick of shape  $(4, 4, 4)$  is given in Fig. 1.

### 2.3 Multiindices from Cartesian indices

In order to utilize the topological algebra shortly recalled in this paper, we need to explicitly sort the cells of the various dimensions into linearly ordered sequences, possibly according to the linear order their information is linearly accommodated in computer storage.

### 2.4 Taubin Smoothing

Every boundary chain extracted from an image block  $\mathbb{B}(i, j, k, n)$  is a 2-cycle, i.e., a closed 2-chain—in other words, a 2-chain with empty boundary. Such 2-cycles are joined together by removing the double 2-cells (at the boundaries of adjacent bricks) after having suitably shifted their indices to an unique linear representation of the whole image. The resulting raster surface is made by mutually orthogonal raster facets, that must be smoothed in order to get a fair surface. A linear time and space algorithm for this purpose is the Laplacian

smoothing, which iteratively moves each vertex (0-cell) to the centroid of its neighbors. A well known weakness of this simple algorithm is the asymptotic convergence of the whole mesh to a single point, resulting in unfair size reduction even after few iterations. Conversely, the Taubin smoothing algorithm [27, 28] alternates two Laplacian smoothing steps with *shrink* and *inflate* effects respectively, with the result of delivering pretty invariant sizes and volume of the smoothed mesh. The best results are obtained on meshes which have small variations of edge length and face angles, like for surfaces extracted from 3D raster images, as in our case.

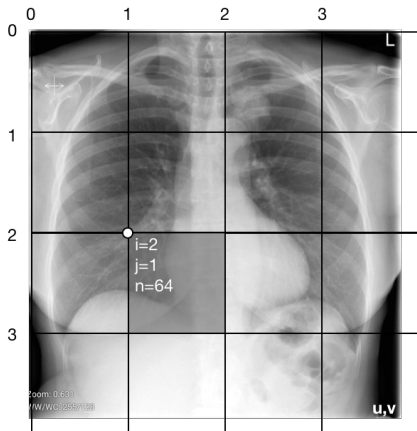
### 3 Brick-parametric design

#### 3.1 Brick decomposition

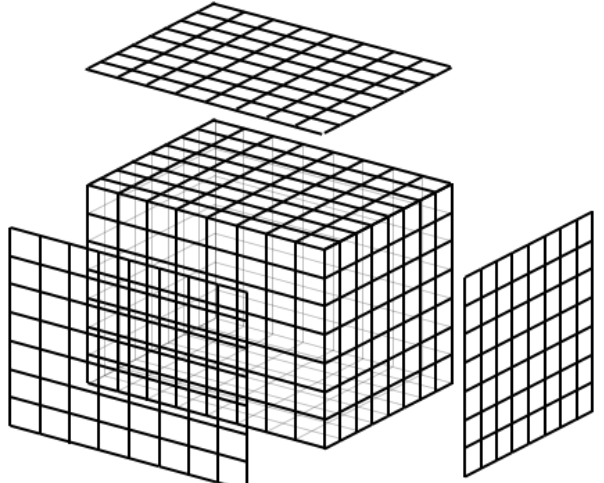
Let us assume that medical devices produce 3D images with lateral dimensions that are integer multiples of some powers of two, like 128, 256, 512, etc. Any cuboidal portion of the image is completely determined by the Cartesian indices of its voxels of lowest and highest indices and extracted by multidimensional array *slicing* as  $\text{image}([\ell_x : h_x, \ell_y : h_y, \ell_z : h_z])$ .

For the sake of simplicity, we assume a common size on the three image axes, and the corresponding image portion  $\mathbb{B}$ , called *brick*, as a function of its element of the lowest brick coordinates  $i, j, k \in [1 : n]$  and the brick lateral size  $n \in \mathbb{N}$ :

$$\mathbb{B}(i, j, k, n) := \text{image}([in : in + n, jn : jn + n, kn : kn + n])$$



(a) A possible brick partitioning of a radiologic image. The evidenced 2D brick, of size  $n^d = 64^2$ , is sliced by  $\mathbb{B}([2, 1, 64]) = \text{Image}([128 : 172], [64 : 128])$



(b) Faces on the brick boundary

**Figure 2:** Brick decomposition

Figure 2a shows the brick decomposition in a 2D image, with positive integers  $(u, v)$  giving the lateral sizes of image. Note that brick sides do not necessarily correspond to image edges.

#### 3.2 Brick operator

##### Chain coordinates

We are going to treat each image brick independently from each other. Hence we map each image brick  $\mathbb{B}(i, j, k, n)$  to the linear *chain* space  $C_2$  of dimension  $n \times n \times n$ , using coordinate vectors  $c \in \mathbf{2}^{n^d} := \{0, 1\}^{n^d}$ ,

where the basis element  $c \in C_2$  is mapped via Cartesian-to-linear map to the binary vector

$$\text{Image}(h, k) \mapsto c_{h,k} := [0 \cdots 0 \ 1 \ 0 \cdots 0] \in \mathbb{B}^{n \times n}$$

for each  $0 \leq h, k \leq n$ , and where the (single) unit element is in position  $nk + h \leq n \times n$ .

Therefore, each pixel (or voxel) in a brick image will be seen as a basis binary vector in  $C_2$ , and each subset of image elements, as the corresponding binary vector in  $C_2$ , with many ones as the cardinality of the subset.

## Boundary operator

For a fixed brick size  $n$ , the boundary operator  $\partial_d : C_d \rightarrow C_{d-1}$ , with  $d \in \{2, 3\}$ , will be constructed once and for all using the algorithm given in [17], and inlined in the generated boundary extraction code.

It is easy to see that the operator's matrix  $[\partial_d]$  is *very sparse*, since it contains  $2 \times d$  non-zero elements (ones) for each column (of length  $n^d$ ), i.e. 4 ones and 6 ones for the 2D and 3D case, respectively. In fact the matrix of a linear operator between linear spaces contains by columns the basis element of the domain space, represented in the target space. In our case, the former is an image element (2-cube or 3-cube), represented as the chain of its boundary—i.e. either a 1-cycle of 4 edges, or a 2-cycle of 6 faces, respectively.

The number of rows of  $[\partial_d]$  equates the dimension of the linear space  $C_{d-1}$ , i.e. the number of  $(d-1)$ -cells—elementary  $(d-1)$ -chains—in the cellular partition of the image. To compute their number, we act in two steps. (a) First we map one-to-one the  $n^d$   $d$ -cells with  $d$  adjacent  $(d-1)$ -cells, so getting  $d n^d$  distinct basis elements of  $C_{d-1}$ . (b) Then we complete this bases by adjoining  $n^{d-1}$  boundary elements for each of the  $d$  dimensions of the image, so providing further  $d n^{d-1}$  basis elements for  $C_{d-1}$ . The dimension of  $C_{d-1}$ , and therefore the number of rows of  $[\partial_d]$  matrix is  $d(n^{d-1} + n^d) = d n(1+n)^{d-1}$ . The number of column equates the number of basis elements of  $C_d$ , i.e. the number  $n^d$  of brick elements.

## Sparsity and size of boundary matrix

As we have seen, we have  $2d$  non-zero elements for each column of  $[\partial_d]$ , so that their total number is  $2dn^d$ . The number of matrix element is  $d n(1+n)^{d-1} \times n^d$ , giving a ratio of

$$\frac{\text{non-zero elements}}{\text{total elements}} = \frac{2d \times n^d}{d n(1+n)^{d-1} \times n^d} = \frac{2}{n + n^d}$$

Using sparse matrices in CSC (Compressed Sparse Column) format we get a storage size:

$$\text{mem}([\partial_d]_{n^d}) = 2 \times \#\text{nz} + \#\text{columns} = 2 \times 2dn^d + n^d = (4d+1)n^d.$$

In conclusion, for brick size  $n = 64$ , the matrix  $[\partial_d]$  requires for 2D images  $9 \times 64^2 = 36,864$  memory elements, and for 3D images  $13 \times 64^3 = 3,407,872$  memory elements. Counting the bytes for the standard implementation of a sparse binary matrix (1 byte for values and 8 bytes for indices) we get  $(18d+8)n^d$  bytes, giving 176 KB for 2D and 15.872 MB for 3D.

### 3.3 Brick boundary mapping

Here we refer directly to the 3D case. Let us call *segment* the bulk content  $S$  of interest within the input 3D image of size  $(u, v, w)$ . Our aim is to compute the segment boundary  $\partial_3 S$ . First we set the size  $n$  of the brick, in order to decompose the input  $\text{Image}(u, v, w)$  into a fair number of bricks

$$M = \lceil u/n \rceil \times \lceil v/n \rceil \times \lceil w/n \rceil \simeq \frac{uvw}{n^3}.$$

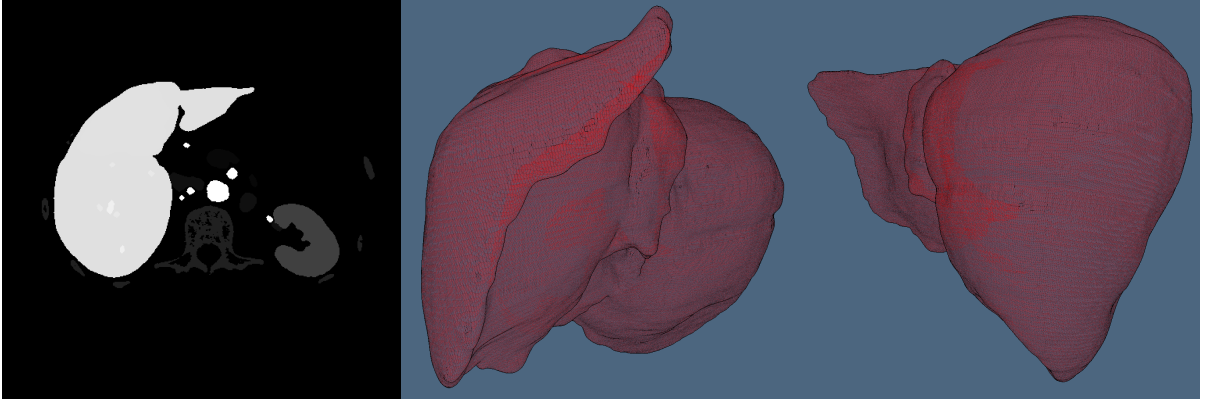


**Figure 3:** The left image shows one slice with segmented organs from the Ircad dataset [25]. The other three images show the surface of the liver and portal vein generated by `lar-surf.jl` package.

Then, we consider each segment portion  $c_{i,j,k} = S \cap \mathbb{B}(i, j, k, n)$  and compute its local coordinate representation  $[c]_{i,j,k} \in C_3(n, n, n)$ . This one is a sparse binary vector of length  $n^3$ . Then, assemble the  $M$  representations  $c$  of segment portions into a sparse binary matrix  $\mathbf{S}$ , of dimension  $n^d \times M$ , with  $d = 3$ . Finally, compute a matrix  $\mathbf{B}$  of boundary portions of  $S$ , represented by columns as chain coordinate vectors in  $C_2$ :

$$\mathbf{B} = [\partial_3(n)] \mathbf{S}.$$

where the boundary matrix has dimension  $n^d \times dn(n+1)^{d-1}$ . Of course, the  $\mathbf{B}$  sparse matrix has the same column number  $M$  of  $\mathbf{S}$ , because each column contains the boundary representation of the corresponding  $S \cap \mathbb{B}(i, j, k, n)$ , and the number of matrix rows is the dimension  $n^d$  of the linear space  $C_2$  of 2-chains.

## Embedding

A final computational step is needed, in order to embed the 2-chains in  $\mathbb{E}^3$  space and to assemble the whole resulting surface. In particular, we need to compute the *embedding function*  $\mu : C_0 \rightarrow \mathbb{E}^3$ , where  $C_0$  is the space of 0-chains, one-to-one with the vertices of the extracted surface. The simplest solution is to associate four 0-cells to each 2-cell of the extracted surface, i.e. to each non-zero entry in every column of  $\mathbf{B}$ . The  $\mu$  function can be computed by identifying, via element position in the column, a triple of integer values  $0 \leq x \leq u$ ,  $0 \leq y \leq v$ , and  $0 \leq z \leq w$  for each vertex of the 2-cell. The mapping can be implemented using a dictionary, that will store the inverse coordinate transformation used at the beginning, i.e. the one from linear to Cartesian coords, in order of not duplicating the output vertices.

## Surface assembling

All boundary surface subsets  $B(i, j, k) = \partial_3 S \cap \mathbb{B}(i, j, k)$ , provided by columns of  $\mathbf{B}$ , are embedded in the same coordinate space. In formal terms, using the standard terminology of LAR scheme:

$$\text{Lar}(S) := (\text{Geom}(S), \text{Top}(S)) = (\mathbf{V}, \mathbf{CV}),$$

where, with respect to the *chain complex*  $C_3 \rightarrow C_2 \rightarrow C_1 \rightarrow C_0$  induced by the input image  $Im$  and segment portion  $S_{i,j,k}$ , we get

$$\text{Geom} := \mu(C_0) = \mathbf{V}, \tag{2}$$

$$\text{Top} := C_3(S) = \mathbf{S} \mapsto \mathbf{CV}. \tag{3}$$

and

$$\text{Lar}(B_{i,j,k}) := (\text{Geom}(B_{i,j,k}), \text{Top}(B_{i,j,k})) = (W, FW), \quad (4)$$

$$\text{Geom} := \mu(C_0(B_{i,j,k})) = W \subset V, \quad (5)$$

$$\text{Top} := C_2(B_{i,j,k}) = \mathbf{B}_{i,j,k} \mapsto FW \subset FV. \quad (6)$$

A translation transformation applied to each vertex subset  $W_{i,j,k}$  with translation vector  $\mathbf{t} = [i, j, k]$  will therefore move it in the final space position, so finally giving

$$\text{Lar}(\mathbf{B}) = \bigoplus_{i,j,k} \text{Lar}(\partial_3 S_{i,j,k}) = \bigoplus_{i,j,k} (W, FW).$$

### 3.4 Brick-level parallelism

In the computational pipeline introduced in this paper, several steps can be efficiently performed in parallel at the image-brick level, depending on the embarrassingly data-parallel nature of the problem. In particular, little effort is needed to separate the problem into a several of parallel tasks  $S_{i,j,k}$ , using multiarray slicing. The granularity of parallelism, depending on the brick size  $n$ , is further enforced by the computation of a single boundary matrix  $[\partial_d(n)]$  depending on  $n$ , so that the initial communication cost of broadcasting the matrix to nodes can be carefully controlled, and finely tuned depending on the system architecture. The whole approach is appropriate for SIMD (Single Instruction, Multiple Data) hybrid architectures of CPUs and GPUs, since only the initial brick setup of boundary matrix and image slices, as well the final collection of computed surface portions, require inter-process communication.

## 4 Julia implementation

The computer code is implemented in Julia language [3] according to the workflow described below, whose stages are parallelized and/or optimized in various ways. The workflow scheme can be seen on Fig. 4. The implementation is available on GitHub [11] and our `LarSurf.jl` package can be installed using a standard Julia package register.

### 4.1 Parallel workflow

#### Workflow setup

The functions in this preliminary step include:

1. the input of 3D medical image  $\mathcal{I}$  with *shape*  $(\ell_1, \ell_2, \ell_3)$ , such that:  $\mathcal{I} = [\ell_1] \times [\ell_2] \times [\ell_3]$ , where  $[\ell_k] = [1, 2, \dots, \ell_k]$ ;
2. analysis of resources available in the computational environment, including operating system, type and number of compute nodes (processors, cores, GPUs), number of cores per node, RAM and caches amounts;
3. depending on the above, best decision for the *size* of 3D image brick  $\mathcal{B}$ . With default *size* = 64, the *number of bricks* will be  $n = \lceil \ell_1 / \text{size} \rceil \times \lceil \ell_2 / \text{size} \rceil \times \lceil \ell_3 / \text{size} \rceil$ . Hence the default number of bricks is  $n = 256$ , for standard images  $512 \times 512 \times 256$ ;
4. computation of Julia's sparse boundary matrix  $[\partial_B]$ , returning a value of type `SparseMatrixCSC{Int8}{Int64}`, where `Int8` and `Int64` are the types for values and indices, respectively, stored by Compressed Sparse Column (CSC) format; the storage of  $[\partial_B]$  (for *size* = 64) requires about 45 MB;

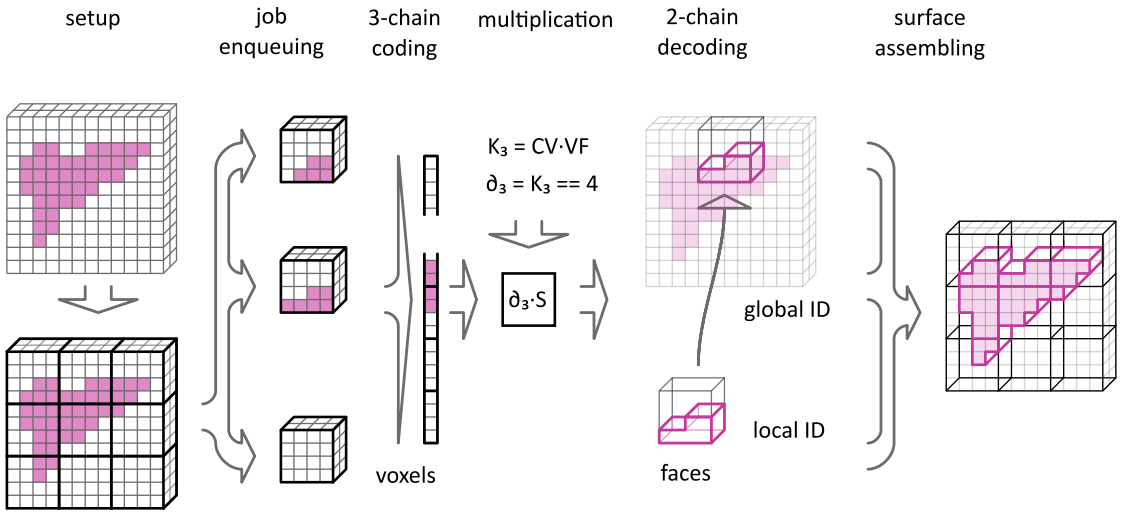


**Figure 4:** Workflow of LAR-SURF algorithm

5. creation of either a local or distributed channel to implement a producer/consumer model of parallel/distributed computation, depending on available resources;
6. distribution of matrix  $[\partial_B]$ , of default size 45 MB, to all available nodes/cores (Julia workers), using the Julia macro `@everywhere`.

With  $\text{size} = 64$ , the number of non-zeros within the sparse matrix  $[\partial(64^3)]$  is  $\text{nnz} = 4792266$ , for a memory size of  $9 \times \text{nnz} + 8 \times 262144 \simeq 45$  MB. The memory size of the sparse matrix is computed by considering 8 + 1 bytes for non-zero element (which are exactly 6 per row), plus 8 bytes per each index of column start.

### Job enqueueing

Communication and data synchronization may be managed through *Channels*, which are the FIFO conduits that may provide producer/consumer communication. Overall execution time can be improved if other tasks can be run while a task is being executed, or while waiting for an external service/function to complete. The single work items of this stage follow:

1. extraction, from image arrays of the block views, depending on 3 Cartesian indices;
2. transform each block *from global*  $[\ell_1] \times [\ell_2] \times [\ell_3]$  to *local coordinates*  $[n] \times [n] \times [n]$ ;
3. further transform of each *foreground voxel*  $v \in \mathcal{S} \subseteq \mathcal{I}$  from Cartesian to linear coordinates, using the suitable Julia's library functions.
4. enqueueing the job (as a sequence of integer positions for the non-zeros image elements aligned in a memory buffer of proper Channel type).

### 3-Chain encoding

The interesting part of the *Image*  $\mathcal{I}$  is called *Segment*  $\mathcal{S}$ . The goal of the whole *workflow* is to extract a *boundary model* of  $\mathcal{S}$  from  $\mathcal{I}$ . The portion of  $\mathcal{S}$  inside  $\mathcal{B}$ , will be denoted as  $\mathcal{S}(\mathcal{B})$ . Each block  $\mathcal{B}$  of the 3D image must be converted into the *coordinate representation* of a vector  $\nu \in C_3$  in the linear space of 3-chains.

In coordinates local to  $\mathcal{B}$ , once fixed an ordering from Cartesian to linear coordinates, this vector is represented by a *binary array* of length *size*<sup>3</sup>. With *size* = 64, we have  $64^3 = 262144$ , with a non-zero value (i.e. 1) for each foreground voxel in  $\mathcal{S}(\mathcal{B})$ . Therefore, the coded segment portion  $\mathcal{S}(\mathcal{B})$  results with a space occupancy of about 262 KB if encoded as a full array (i.e. including the zero values). Whether encoded as a sparse vector, its space occupancy will correspondingly decrease.

1. each encoding task produces either a full or sparse binary vector. With full or sparse arrays depending by one index, we get either 262 KB or less per job, correspondingly;
2. special format for sparse CSC (Compressed Sparse Column) vectors can be used, since the *value* data for non-zeros does not need storage. Hence only a single 1-array of Int64 row positions (with total length equal to the number of non-zeros in the block, with  $8 \times \text{nnz}$  kB storage) is needed;
3. prepare subsequences of such data vectors (non-zero linear row indices), in order to feed efficiently the available processor threads. In case of the presence of one/more GPUs, a smaller size of the block—and hence of the boundary matrix and the encoded 3-chain vectors—and then much higher vector numbers, are preferable for speed.

### SpMM Multiplication

According to the current literature [4] it is more convenient to execute SpMV (sparse matrix-vector) multiplications than SpMSpV (sparse matrix-sparse vector) multiplications. Since we have 256 such jobs (one multiplication per block) to perform in the default setting of the algorithm (the size of the block  $64^3$ ; the size of the image  $512^2 \times 256$ ), or more in case of either smaller blocks or image greater than the standard one, this stage must be evidently parallelized and carefully tuned, possibly by using the GPU, if available.

1. Various multiplication algorithms are being tested, using several packages for sparse linear algebra and/or custom implementations;
2. the total speed of this stage will strongly depend on the hardware available, on the granularity of blocks, and on the choice between dense/sparse storage of encoded 3-chains;
3. anyway, the compute elements or threads will be fed without solution of continuity in a *dataflow* process. This parallel operation is, according to our preliminary experiments, the critical one of the whole workflow, in the sense that any  $\Delta T$  (either positive or negative) in this stage will contribute to the total time  $T$ .

### 2-Chain decoding

Each multiplication of  $[\partial_B] : C_3 \rightarrow C_2$ , times a 3-chain  $\nu \in C_3$ , produces a 2-chain  $\sigma \in C_2$ , i.e. the *coordinate representation* of the *boundary vector*  $\sigma \in C_2$ . The inverse of the coding algorithm is executed in the present stage. This process can also be partially superimposed in time with the previous ones, depending on the size of the memory buffers used to feed the CPU cores or the GPUs and get their results. Some elementary steps follow:

1. conversion from the position of ones (or non-zeros) in the 2-chain to linear indices of rows;

2. conversion from linear indices to Cartesian indices in coordinates local to the  $\mathcal{B}$  block, using the appropriate library functions;
3. conversion from each Cartesian index value to a suitably oriented (i.e. with proper attitude) geometry quadrilateral (or pair of triangles) in local coordinates.

Julia's vectorized pipeline dataflow seems the more appropriate implementation model for the job of each worker.

### Assembling and artifact filtering

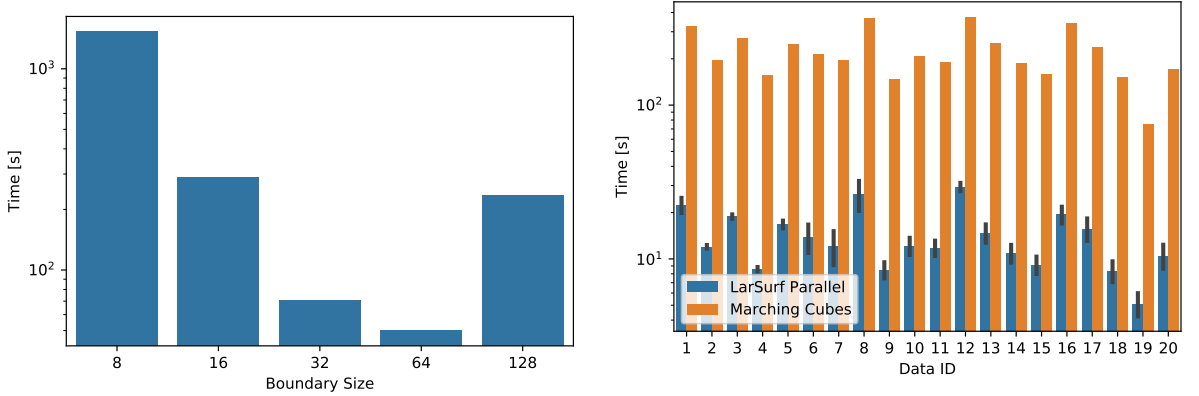
The results of the previous stages can be described as a *collection of sets of geometric quadrilaterals (quads)*, each one encoded as an array of quadruples of integer indices, pointing to the linear array of grid vertices associated to the image block  $\mathcal{B}$ . In other words, *all quads of each job* are now given in the **same local coordinates**. Besides putting each partial surface  $\mathcal{S}(\mathcal{B}) = (\mathbf{V}_\mathcal{B}, \mathbf{FV}_\sigma)$  in the global coordinate system of the image, the present stage must eliminate the redundant boundary features possibly generated at the edges of the partial surface  $\mathcal{S}(\mathcal{B})$  within each block  $\mathcal{B}$  such that  $\mathcal{B} \cap \mathcal{I} \neq \emptyset$ :

1. translate each array  $\mathbf{FV}_\sigma$ , of type `Lar.Cells`, by summing to each vertex index the linearized offset of the Cartesian coordinates  $(n, m, p)(\mathcal{B})$  of the  $\mathcal{B}$ 's reference vertex, i.e. the one with (all) lowest *Cartesian coordinates* within the  $\mathcal{B}$  block.
2. remove both instances of *double quads* generated by `Lar` software at the block boundaries (see Fig. 2b). They are artifacts generated by the decomposition of the whole image into a number of blocks of tractable size.
3. a smart strategy of removal of such artifacts may be used, which does not require any sorting nor searching on the assembled array of quads. It will consist in arranging each block with all three dimensions decreased-increased by one so that each 2-adjacent pair of blocks will be covering each other for a full side extent of blocks of depth one.

### Smoothing

The final smoothing of the generated surfaces cannot be performed block-wise since this would introduce smoothing artifacts at the block boundaries. Anyway, the Taubin smoothing [26] can be performed in parallel, since for each vertex in the final surface (except eventually the ones on the image  $\mathcal{I}$  boundaries) it essentially consists in computing a new position as a proper average of its neighborhood vertices, i.e. by applying a discrete Laplacian operator. Some appropriate sets of workers may so be assigned the task of generating iteratively a new position for the vertices they take care of. In particular, we have:

1. Job enqueueing, by writing sets of integers (global linear indices of vertices) in array buffers of type `Channel`;
2. vectorized computation of proper averages of near vertices;
3. job dequeuing, by recovering finished tasks from a channel and assembling the results into the embedding function  $V : C_0 \rightarrow \mathbb{E}^3$ , providing an array of type `Lar.Points` of `Float64 × 3`, with vertex coordinates by column.



(a) Time requirements of the LAR-SURF filter used on artificial volumetric data with various sizes of boundary matrix  
(b) Time requirements of the LAR-SURF filter and Marching Cubes on the Ircadb dataset. Error bars show the 95% confidence interval

**Figure 5:** Performance analysis of the LAR-SURF filter.

## 4.2 Performance analysis

### Boundary matrix size

The size of the boundary matrix is a critical parameter of the LAR-SURF method. To determine optimal size of boundary matrix the experiment on artificial data was performed (Fig. 5a). The size of experimental data is set to  $512 \times 512 \times 512$  and it is derived from a typical size of Computed Tomography medical images. Computation is done on the Tesla DGX-1 machine.

According to the experiment the fastest computation is with the boundary matrix with size  $64 \times 64 \times 64$ . This is an expected result. The larger boundary matrix is too big to fit in CPU's cache memory.

### Comparison with the Marching Cubes algorithm

To compare the time requirements of LAR-SURF with Marching Cubes implemented in Python we performed an experiment on Ircadb dataset [24]. Dataset contain 20 Computed Tomography images (see table 1) with xy-resolution from 0.56 mm to 0.87 mm and z-resolution from 1.0 mm to 4.0 mm. The number of slices is each series varies from 74 to 260 and the size of each slice is  $512 \times 512$ . The dataset contains manually segmented liver, portal vein, and other structures. We performed surface extraction of the liver with Marching Cubes and LAR-SURF. The time required for computation can be seen in Fig. 5b.

Based on the t-test with  $\alpha = 0.99$ ,  $p = 8.735 \times 10^{-24}$  and  $s = -16.67$  it can be shown that the mean of time consumed by LAR-SURF is significantly lower from time consumed by Marching Cubes.

## 5 Examples

Use of the `LarSurf.jl` package can be seen on listings 1 where the liver segmentation with 2865131 voxels from the Ircadb dataset is used as an input for our surface extraction algorithm. The size of 3D volumetric image is  $129 \times 512 \times 512$  and the voxel resolution is  $1.6 \times 0.57 \times 0.57$  [mm]. The output liver surface model is formed by 182124 triangles and the number of vertices is 90822. The visualization can be seen in Fig. 6.

**Listing 1:** Get surface from DICOM volumetric data

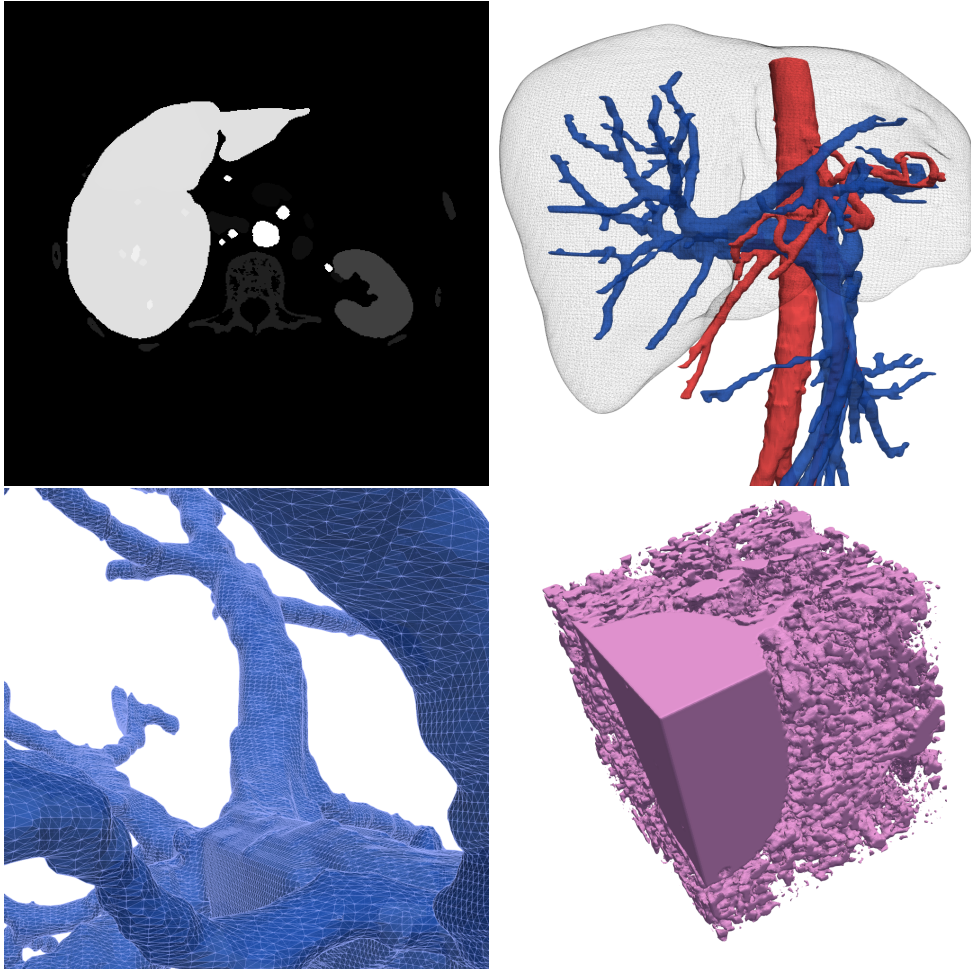


**Figure 6:** Liver structures. The upper left image shows one slice with segmented organs from the Ircad dataset [24]. The other images show the triangulated isosurfaces of the macroscopic and microscopic structures of the liver extracted with LAR-SURF algorithm. The wireframe model of the human liver along with the portal vein and hepatic artery can be seen on the upper right image. The left bottom image shows the detail of the portal vein with resolution  $1.6 \times 0.57 \times 0.57$  [mm]. On the bottom right image is shown the microvasculature of a pig liver based on corrosion cast prepared by Eberlova [10]. The size of the specimen is 0.936 [mm] along each axis and the resolution of the Micro-CT data is  $4.682 \mu\text{m}$ .

```

using Distributed
using Pio3d # Read 3D data from DICOM files
addprocs(3) # set number of processors
using LarSurf

LarSurf.lsp_setup([64, 64, 64]) # set block size

# read data from DICOM files
datap = Pio3d.read3d("3Dircadb1.1/MASKS_DICOM/liver")
segmentation = datap["data3d"]
voxelsize_mm = datap["voxelsize_mm"]

# get surface
V, FV = LarSurf.lsp_get_surface(segmentation, voxelsize_mm)
FVtri = LarSurf.triangulate_quads(FV)

# do smoothing and save data
Vs = LarSurf.Smoothing.smoothing_FV_taubin(V, FV, 0.5, -0.2, 40)
objlines = LarSurf.Lar.lar2obj(Vs, FVtri, "liver.obj")

```

The portal vein surface extraction can be performed with a small change of input path in code. The 3D image resolution is the same. The number of input voxels is 103533. The output surface is created by 90822 vertices and 182124 triangles.

The right bottom image of Fig. 6 is the surface of the microvasculature of pig liver. The volumetric image is based on Micro-CT data of corrosion casts of pig liver. [10]. The size of the visualized data is  $100 \times 100 \times 100$  voxels and the size of the voxel is  $4.682 \mu\text{m}$ . The number of triangles is 544784 and the number of vertices is 272826.

## 6 Conclusion

We introduced a Julia implementation of an algebraic filter to extract from 3D medical images the boundary surface of some specific image segment, described as a 3-chain of voxels. Translations from Cartesian indices of cells to linearized indices, the computation of the sparse boundary matrices, and the sparse matrix-vector multiplication are the main computational kernels of this approach.

The implementation of the LAR-SURF filter is available in the open-source repository and it can be installed using standard Julia package manager [11].

We showed a good speed-up over marching-cubes algorithms. The existing implementation employs Julia's channels for multiprocessing. Our performance experiment showed an optimal size of the brick size. Parallelization makes a large portion of spared computational cost. Moreover, we expect additional improvement in the future because our approach is appropriate for SIMD (Single Instruction, Multiple Data) hybrid architectures of CPUs and GPUs, since only the initial block setup of boundary matrix and image slices, as well the final collection of computed surface portions, require inter-process communication.

Currently, the computational pipeline is being strongly improved to gain a greater speed-up using native Julia implementation CUDA.jl of Nvidia programming platform [2], and Julia's SuiteSparseGraphBLAS.jl framework [4] for graph algorithms with the language of linear algebra. In particular, we are extending its use pattern in order to work with general cellular complexes.

## ACKNOWLEDGEMENTS

This work was supported by Charles University Research Centre program UNCE/MED/006 "University Center of Clinical and Experimental Liver Surgery" and Ministry of Education project ITI CZ.02.1.01/0.0/0.0/17\_048/0007280: Application of modern technologies in medicine and industry. The research was also supported by the project LO 1506 of the Czech Ministry of Education, Youth and Sports.

## A Appendix

### 1.1 Symbol list

$\mathcal{I}$  three-dimensional medical image

$\ell_1, \ell_2, \ell_3$  dimensions of image

$\mathcal{S}$  segment: a subset of voxels from image segmentation

$\mathcal{B}$  3D image brick

*size* lateral dimension of cubic brick  $\mathcal{B}$

$n$  number of bricks  $\mathcal{B}$  (jobs) in  $\mathcal{I}$

$[\partial_{\mathcal{B}}]$  boundary matrix for brick  $\mathcal{B}$

$C_p$  linear (vector) space of  $p$ -chains

$\nu \in C_p$   $p$ -chain

$[\nu]$  coordinate representation (binary vector) of  $\nu$

$\mathbb{E}^3$  Euclidean 3-space

### 1.2 Definitions

**Boundary model** Closed manifold surface of the boundary of a solid model

**CSC** Compressed Sparse Column format for sparse matrices

**Global coordinates** Integer linear coordinates of  $\mathcal{I}$

**Local coordinates** Integer linear coordinates of  $\mathcal{B}$

**Cartesian coordinates** Integer triples  $(i, j, k)$  one-to-one with voxels

**Voxels** Individual elements in 3D image (3-cells)

**$p$ -chain** Formal linear combination of  $p$ -cells with coefficients in  $\{0, 1\}$

**Coord. repr.** Binary vector (for  $p$ -chains) or binary matrix (for chain operators)

**Quad** Geometric quadrilateral; convex polygon with four vertices

**Foreground voxel** Individual element of a segment  $\mathcal{S}$

**Segment** Subset of voxels resulting from image segmentation

### 1.3 3D-Ircadb Dataset

For performance analysis the public dataset from Research Institute against Digestive Cancer (IRCAD) [24] was used. The table 1 describe the dataset.

	z-resolution [mm]	xy-resolution [mm]	obj. voxels	size xy	size z
min	1.00000	0.561000	5.832080e+05	512.0	74.000000
mean	1.77750	0.725141	1.894777e+06	512.0	141.150000
50%	1.60000	0.739094	1.760604e+06	512.0	127.000000
max	4.00000	0.873047	3.341433e+06	512.0	260.000000

**Table 1:** Ircad dataset description [24]. It contains 20 Computed Tomography images of abdomen with manually segmented tissues.

### 1.4 Basic operations in LAR

#### Boundary matrices for grids of cubes:

We give here the full Julia code for the algebraic computation of  $\partial_3$  matrix, for a very little grid of unit 3-cubes. Due to the simplicity of the cells (voxels = cubes), a sufficient (geom,top) pair is given below as ( $V, CV$ ), where  $CV$  is an array of arrays of Float64 indices of grid cubes.

```
julia> using LinearAlgebraicRepresentation, SparseArrays
julia> Lar = LinearAlgebraicRepresentation
julia> V, CV = Lar.cuboidGrid([3,2,1])
julia> V
0.0 0.0 0.0 0.0 0.0 0.0 1.0 1.0 1.0 1.0 1.0 2.0 2.0 2.0 2.0 2.0 2.0 3.0 3.0 3.0 3.0 3.0 3.0 3.0
0.0 0.0 1.0 1.0 2.0 2.0 0.0 0.0 1.0 1.0 2.0 2.0 0.0 0.0 1.0 1.0 2.0 2.0 0.0 0.0 1.0 1.0 2.0 2.0
0.0 1.0 0.0 1.0 0.0 0.0 1.0 0.0 0.0 1.0 0.0 0.0 1.0 0.0 0.0 1.0 0.0 0.0 1.0 0.0 0.0 1.0 0.0 1.0
julia> CV
[[ 1, 2, 3, 4, 7, 8, 9,10], [ 3, 4, 5, 6, 9,10,11,12], [ 7, 8, 9,10,13,14,15,16],
 [ 9,10,11,12,15,16,17,18], [13,14,15,16,19,20,21,22], [15,16,17,18,21,22,23,24]]
```

#### Face and Edge Data generation:

In the following, we provide the functions for generating the face data  $FV$  (vertex indices in faces) with function  $CV2FV$  and edge data  $EV$  (vertex indices in edges) with function  $CV2EV$  from cell data  $CV$ .

```
function CV2FV( v:: Array{ Int64 } )
    return faces = [[v[1], v[2], v[3], v[4]], [v[5], v[6], v[7], v[8]],
                    [v[1], v[2], v[5], v[6]], [v[3], v[4], v[7], v[8]],
                    [v[1], v[3], v[5], v[7]], [v[2], v[4], v[6], v[8]]]
end
function CV2EV( v:: Array{ Int64 } )
    return edges = [[v[1],v[2]], [v[3],v[4]], [v[5],v[6]], [v[7],v[8]], [v[1],v[3]], [v[2],v[4]],
                    [v[5],v[7]], [v[6],v[8]], [v[1],v[5]], [v[2],v[6]], [v[3],v[7]], [v[4],v[8]]]
end
```

#### Characteristic matrices:

The function K transforms an array of arrays (VV, EV, FV, CV) into a sparse binary characteristic matrix ( $M_0, M_1, M_2, M_3$ ). A Julia sparse matrix needs three arrays I, J, Vals of rows, columns, values of non-zeros:

```
VV = [[v] for v=1:size(V, 2)];
VV = collect(Set{Array{Int64,1}}(vcat(map(CV2FV, CV)...)))
[[13,15,19,21], [1,2,3,4], [7,9,13,15], [13,14,15,16], [7,8,13,14], [1,2,7,8], [2,4,8,10], [7,8,9,10],
[3,5,9,11], [8,10,14,16], [15,16,21,22], [9,11,15,17], [3,4,5,6], [17,18,23,24], [11,12,17,18],
[1,3,7,9], [3,4,9,10], [9,10,15,16], [4,6,10,12], [13,14,19,20], [9,10,11,12], [15,16,17,18],
[19,20,21,22], [15,17,21,23], [16,18,22,24], [21,22,23,24], [10,12,16,18], [5,6,11,12], [14,16,20,22]]

EV = collect(Set{Array{Int64,1}}(vcat(map(CV2EV, CV)...)))
[[15,17], [16,22], [6,12], [17,23], [18,24], [4,10], [3,4], [13,15], [11,12], [9,15], [13,19],
[1,7], [5,11], [5,6], [12,18], [8,14], [15,21], [17,18], [1,3], [2,4], [16,18], [2,8], [21,23],
[20,22], [1,2], [14,16], [10,16], [13,14], [19,21], [7,13], [9,10], [23,24], [11,17], [21,22],
[3,9], [3,5], [9,11], [7,9], [14,20], [7,8], [22,24], [19,20], [8,10], [15,16], [10,12], [4,6]]

function K(CV)
    I = vcat( [ [k for h in CV[k]] for k =1: length(CV) ]...)
    J = vcat(CV ...)
    Vals = Int8[1 for k=1: length(I)]
    return SparseArrays.sparse(I,J,Vals)
end
M0 = K(VV); M1 = K(EV); M2 = K(FV); M3 = K(CV)
```

### Boundary matrices:

The boundary matrices between non-oriented chain spaces are computed by sparse matrix multiplication followed by matrix filtering, produced in Julia by the broadcast of vectorized integer division ( $\div$ ):

```
# This code is working with Julia 1.2
partial_1 = M0 * M1'
partial_2 = div.((M1 * M2'), 2)
s = sum(M2, dims=2)
partial_3 = (M2 * M3') ./ s
partial_3 = div.(partial_3, 1)
```

### ORCID

Miroslav Jirik  <http://orcid.org/0000-0002-8002-2079>  
Alberto Paoluzzi  <http://orcid.org/0000-0002-3958-8089>

### REFERENCES

- [1] Bajaj, C.L.; Pascucci, V.; Thompson, D.; Zhang, X.Y.: Parallel accelerated isocontouring for out-of-core visualization. Proceedings of the 1999 IEEE Symposium on Parallel Visualization and Graphics, PVGS 1999, 97–104, 1999. <http://doi.org/10.1145/328712.319342>.
- [2] Besard, T.; Foket, C.; De Sutter, B.: Effective Extensible Programming: Unleashing Julia on GPUs. IEEE Transactions on Parallel and Distributed Systems, 30(4), 827–841, 2019. ISSN 15582183. <http://doi.org/10.1109/TPDS.2018.2872064>.
- [3] Bezanson, J.; Edelman, A.; Karpinski, S.; Shah, V.B.: Julia: A fresh approach to numerical computing. SIAM Review, 59(1), 65–98, 2017. <http://doi.org/10.1137/141000671>.
- [4] Buluc, A.; Mattson, T.; McMillan, S.; Moreira, J.; Yang, C.: Design of the GraphBLAS API for C. In Proceedings - 2017 IEEE 31st International Parallel and Distributed Processing Symposium Workshops, IPDPSW 2017, 643–652, 2017. ISBN 9781538634080. <http://doi.org/10.1109/IPDPSW.2017.117>.

- [5] Chernyaev, E.: Marching cubes 33: Construction of topologically correct isosurfaces. Tech. rep., 1995. <http://wwwinfo.cern.ch/asdoc/psdir>.
- [6] Crossno, P.; Angel, E.: Isosurface extraction using particle systems. Proceedings of the IEEE Visualization Conference, 495–498, 1997. <http://doi.org/10.1109/visual.1997.663930>.
- [7] Custodio, L.; Pesco, S.; Silva, C.: An extended triangulation to the Marching Cubes 33 algorithm. Journal of the Brazilian Computer Society, 25(1), 6, 2019. ISSN 1678-4804. <http://doi.org/10.1186/s13173-019-0086-6>.
- [8] Dicarlo, A.; Milicchio, F.; Paoluzzi, A.; Shapiro, V.: Chain-based representations for solid and physical modeling. IEEE Transactions on Automation Science and Engineering, 6(3), 454–467, 2009. ISSN 15455955. <http://doi.org/10.1109/TASE.2009.2021342>.
- [9] Dicarlo, A.; Paoluzzi, A.; Shapiro, V.: Linear algebraic representation for topological structures. Comput. Aided Des., 46, 269–274, 2014. ISSN 0010-4485. <http://doi.org/10.1016/j.cad.2013.08.044>.
- [10] Eberlova, L.; Liska, V.; Mirka, H.; Tonar, Z.; Havíř, S.; Svoboda, M.; Benes, J.; Palek, R.; Emingr, M.; Rosendorf, J.; others: The use of porcine corrosion casts for teaching human anatomy. Annals of Anatomy-Anatomischer Anzeiger, 213, 69–77, 2017.
- [11] Jirík, M.; Paoluzzi, A.: LarSurf.jl package on GitHub, 2020. <https://mjirik.github.io/LarSurf.jl/>.
- [12] Lachaud, J.O.; Montanvert, A.: Continuous analogs of digital boundaries: A topological approach to iso-surfaces. Graphical Models, 2000. ISSN 15240703. <http://doi.org/10.1006/gmod.2000.0522>.
- [13] Lorensen, W.E.; Cline, H.E.: Marching Cubes: A High Resolution 3D Surface Construction Algorithm. ACM siggraph computer graphics, 21(4), 163–169, 1987.
- [14] Natarajan, B.K.: On generating topologically consistent isosurfaces from uniform samples. The Visual Computer, 11(1), 52–62, 1994. ISSN 1432-2315. <http://doi.org/10.1007/BF01900699>.
- [15] Newman, T.S.; Yi, H.: A survey of the marching cubes algorithm. Computers and Graphics (Pergamon), 30(5), 854–879, 2006. ISSN 00978493. <http://doi.org/10.1016/j.cag.2006.07.021>.
- [16] Paoluzzi, A.; Dicarlo, A.; Furiani, F.; Jirík, M.: CAD models from medical images using LAR. Computer-Aided Design, 13(6), 2016. ISSN 0010-4485. <http://doi.org/10.1080/16864360.2016.1168216>.
- [17] Paoluzzi, A.; Shapiro, V.; DiCarlo, A.; Furiani, F.; Martella, G.; Scorzelli, G.: Topological computing of arrangements with (co)chains. Transactions on Spatial Algorithms and Systems (ACM TSAS). Accepted for publication.
- [18] Paoluzzi, A.; Shapiro, V.; DiCarlo, A.; Scorzelli, G.; Onofri, E.: Finite Boolean Algebras for Solid Geometry using Julia's Sparse Arrays. arXiv e-prints, arXiv:1910.11848, 2019. <https://arxiv.org/pdf/1910.11848.pdf>.
- [19] Paoluzzi, A.; Shapiro, V.; DiCarlo, A.; Scorzelli, G.; Onofri, E.: Finite boolean algebras for solid geometry using julia's sparse arrays, 2019. <https://arxiv.org/abs/1910.11848>. Eprint in <https://arxiv.org/abs/1910.11848>.
- [20] Requicha, A.G.: Representations for rigid solids: Theory, methods, and systems. ACM Comput. Surv., 12(4), 437–464, 1980. ISSN 0360-0300. <http://doi.org/10.1145/356827.356833>.
- [21] Rohan, E.; Lukes, V.; Jonášová, A.: Modeling of the contrast-enhanced perfusion test in liver based on the multi-compartment flow in porous media. Journal of Mathematical Biology, 77(2), 421–454, 2018. ISSN 14321416. <http://doi.org/10.1007/s00285-018-1209-y>.
- [22] Shapiro, V.: Solid modeling. In G. Farin; J. Hoschek; S. Kim, eds., Handbook of Computer Aided Geometric Design, chap. 20, 473–518. Elsevier Science, 2002.

- [23] Smistad, E.; Elster, A.C.; Lindseth, F.: Real-Time Surface Extraction and Visualization of Medical Images using OpenCL and GPUs. In Norsk informatikkonferanse, 141–152, 2012. <http://www.tapironline.no/last-ned/1050>.
- [24] Soler, L.: 3D-IRCADb-01 dataset, 2016. <https://www.ircad.fr/research/3dircadb/>.
- [25] Soler, L.: 3D-IRCADb-01 (<http://www.ircad.fr/research/3d-ircadb-01/>), 2016. <http://www.ircad.fr/research/3d-ircadb-01/>.
- [26] Taubin, G.: Curve and surface smoothing without shrinkage, 1995. <http://doi.org/10.1109/iccv.1995.466848>.
- [27] Taubin, G.: A signal processing approach to fair surface design. In Proceedings of the 22Nd Annual Conference on Computer Graphics and Interactive Techniques, SIGGRAPH '95, 351–358. ACM, New York, NY, USA, 1995. ISBN 0-89791-701-4. <http://doi.org/10.1145/218380.218473>.
- [28] Taubin, G.: Geometric Signal Processing on Polygonal Meshes. In Eurographics 2000 - STARs. Eurographics Association, 2000. ISSN 1017-4656. <http://doi.org/10.2312/egst.20001029>.